Tunable and miniaturized microwave filters using carbon nanotube-based variable capacitors

Tunable and miniaturized microwave filters using carbon nanotube-based variable capacitors

Martino Aldrigo, *Member, IEEE*, Mircea Dragoman, Sergiu Iordanescu, *Life Member, IEEE*, George Boldeiu, Paolo Crippa, *Senior Member, IEEE*, Giorgio Biagetti, *Member, IEEE*, Claudio Turchetti, *Life Member, IEEE*, Luca Pierantoni, *Senior Member, IEEE*, Davide Mencarelli, *Member, IEEE*, Stephane Xavier, Laurent Gangloff, and Afshin Ziaei

***Abstract*—In this paper, we introduce a novel concept of tunable and miniaturized filters which embed, as voltage-controlled elements, state-of-the-art variable capacitors, based on vertically aligned carbon nanotubes (VACNTs). Starting from a theoretical estimation of the voltage-dependent capacitance between two adjacent CNTs, we extended this physics principle to a large matrix of CNTs, suitably placed on the molybdenum electrodes of an interdigitated capacitor (IDC), since molybdenum can withstand the high temperature necessary in the plasma process for the growth of the VACNTs. The IDC is the tunable element of a microwave filter, which must fulfill the need for both reconfigurability (being either a low-pass, a high-pass or a band-pass filter, at discretion) and low-voltage frequency tuning of reflection/transmission coefficients. For all these reasons, a very compact layout made of T-type cells (comprising VACNT-based variable capacitors and distributed inductors) was designed, simulated, fabricated, and tested, targeting the C, X, and K_u bands (4–16 GHz) for wireless and radar applications. Taking as a reference the free-space wavelength λ_0 at 10 GHz, the band-pass filter has overall dimensions of just 3.19 mm × 3.47 mm (i.e., $0.11\lambda_0 \times 0.12\lambda_0$), with the minimum of the reflection coefficient shifting of 1.16 GHz (within the X band) for an applied dc bias voltage of just 4 V and spanning between -24.81 dB and -36.13 dB. Furthermore, the maximum rejection is 31.65 dB, and the 3-dB fractional bandwidth is 12.44%. The proposed filters are the proof that nanomaterials can be profitably integrated into microwave components for next-generation transceivers.**

***Index Terms*—Microwave filters, tunable circuits and devices, carbon nanotubes, nanotechnology, nanoelectromechanical systems.**

I. Introduction[1]

MICROWAVE filters are ubiquitous components of utmost importance in many areas of modern wireless and telecommunications systems [1], as they guarantee that only the high-frequency signal in a selected band of interest can be transmitted or received with a predefined amount of power. A very important branch for passive devices is represented by frequency tunable filters [2], [3], covered by a huge scientific literature. The tunability can be realized by different techniques, e.g., tunable Fabry-Perot interferometers, acousto-optic tunable filters (AOTF) formed by bonding piezoelectric transducers (such as lithium niobate) to an anisotropic birefringent medium [4], material-filled active fibers [5], MEMS variable capacitors [6], [7], active-R filters [8], semiconductor varactors and ferroelectric capacitors [9]–[18], and other innovative techniques [19]–[22]. Frequency tunability has to be achieved taking three main issues into account: (i) the variation of the unloaded Q-factor (Q_u) of the basic tunable resonator, due to a voltage- and/or frequency-dependent change of its equivalent resistance, inductance, and capacitance (this variation affects directly the insertion loss (*IL*) in the band of interest); (ii) the frequency tuning range, which depends strongly on the tuning range of the varactor/capacitor; (iii) the harmonic suppression [23]. Another concern is given by miniaturization (and successive integration), since deeply sub-wavelength filters exhibit high losses and undesired parasitic effects with respect to off-the-shelf bulk components. Hence, a major drawback of miniaturized filters is represented by high values of *IL*, which often require a post-amplification stage [24]. On the other hand, carbon-based nanoelectronics has been attracting an increasing interest since the discovery of graphene (and related materials). The modern (and future) trend is a tight interdisciplinary connection between materials science, nanotechnology, and microwaves, thus leading to radically new solutions that comply with the need for devices with much smaller size and extended functionalities with respect to what can be achieved with today's silicon technologies [25]. Carbon nanotubes (CNTs) are one of the materials that could be exploited to achieve this goal: metallic/semiconducting CNTs exhibit unique physical and electronic properties [26] that have been studied extensively in the last years. CNTs represent a very promising technology for various microwave applications, such as diodes, FETs,

This work was supported by the European Project H2020 ICT-07-201 NANOSMART, Grant No. 825430.

M. A., M. D., S. I., and G. Bo. are with the National Institute for Research and Development in Microtechnologies, IMT-Bucharest, 126A Erou Iancu Nicolae Street, 077190 Voluntari (Ilfov), Romania (e-mail: {martino.aldrigo; mircea.dragoman; sergiu.iordanescu; george.boldeiu}@imt.ro). P. C., G. Bi., C. T., L. P., and D. M. are with Università Politecnica delle Marche, Via Brecce Bianche 12, 60131 Ancona, Italy (e-mail: {p.crippa; g.biagetti; c.turchetti; l.pierantoni; d.mencarelli}@staff.univpm.it). S. X., L. G., and A. Z. are with Thales R&T France, Campus Polytechnique, 1 avenue Augustin Fresnel, 91767 Palaiseau Cedex, France, (e-mail: {stephane.xavier; laurent.gangloff; afshin.ziaei}@thalesgroup.com).

interconnections, sensors, composite materials, microscopy, etc. Referring to varactors and variable capacitors, CNTs could offer substantial improvements with respect to semiconductors, since they offer higher cut-off frequencies and lower losses [27]. However, despite some attempts to model and validate CNT-based variable capacitors and phase shifters [28]–[30], a very first example of CNT-based microwave filter was presented in [31], even if the effect of the frequency tuning was quite negligible and the CNT matrix was much bigger and denser (hence, more prone to fabrication defects).

In this paper, we go beyond the actual state-of-the-art in the domain of variable capacitors based on CNTs. More in detail, we validate a proof-of-concept microwave filter for wireless applications covering the C, X, and K_u bands (4–16 GHz), and in which the frequency tuning is obtained by simply applying the proper dc bias voltage to the signal lines of a coplanar waveguide (CPW) structure, suitably designed to host a reconfigurable filter comprising molybdenum interdigitated capacitor (IDC), on top of which a dense matrix of metallic vertically aligned CNTs (VACNTs) was grown. The manuscript is organized as follows. Section II presents a rigorous theoretical model of the capacitance between two VACNTs, followed by multi-physics simulations validating the concept of CNT-based variable capacitor. Then, in Section III we provide (i) the circuit design of both CNT-based IDC and filters, and (ii) the circuit- and 3D full-wave electromagnetic (EM)-based simulations of the filters, together with a discussion about the influence of the different components on the overall performance. Section IV is dedicated to the detailed fabrication process. Finally, in Section V we show the complete dc and RF characterization of the CNT-based filters. Conclusions and future perspectives are given at the end.

II. Theoretical Model and Multi-physics Simulations of the VACNT-Based Variable Capacitor

A. Theoretical Model of the Capacitance of a VACNT Matrix

In the proposed VACNT-based variable capacitor, the basic concept is the electrostatic tuning of the capacitance by means of attractive and repulsive forces between adjacent nanotubes in the array. For this reason, the proposed component can be categorized as a nanoelectromechanical system (NEMS), in which the mechanical actuation is realized by two external dc bias voltages of opposite sign, thus providing a change of the capacitance between two oppositely polarized VACNTs. Fig. 1 is a 3D schematic of this concept.

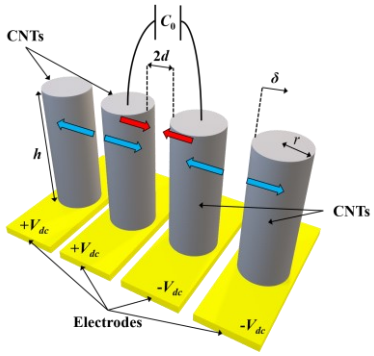

Fig. 1. 3D schematic of the VACNT-based variable capacitor. The red and blue arrows represent attractive and repulsive Coulomb forces, respectively.

Let us consider two adjacent pairs of VACNTs, the CNTs of each pair being biased by the same external dc voltage (one pair by "$+V_{dc}$" and the other by "$-V_{dc}$"), h is the height of the CNTs, r their radius, $2d$ the distance between two oppositely biased nanotubes, δ the displacement of the tip of each nanotube with respect to its unbiased position, and C_0 the capacitance between two oppositely polarized CNTs (see Fig. 1). C_0 is a function of the dc bias voltage V_{dc}: this capacitance is the target of the theoretical model described in this paragraph. Let us define the following quantities: F_{tot} is the total electrostatic force (comprising attractive and repulsive Coulomb components due to all the other nanotubes in different rows); E is the Young's modulus of a CNT; $I = \pi r^4/4$ is the momentum of inertia of the CNT with radius r; m and n are the number of rows and columns of the VACNT matrix, respectively; C_{tot} is the total capacitance of the VACNT matrix. The following equations can be defined for δ, C_0, and C_{tot} [27]:

$$\delta(V_{dc}) = F_{tot}(V_{dc})h^3/(3EI) \quad (1)$$

$$C_0(V_{dc}) = \frac{2\pi\varepsilon_0}{cosh^{-1}\{[d-\delta(V_{dc})]/r\}} 0.85[(d+r)^2 r]^{1/3} \quad (2)$$

$$C_{tot}(V_{dc}) = C_0(V_{dc})\, mn/2. \quad (3)$$

With these equations, it is possible to give a rough theoretical estimation of $C_0(V_{dc} = 0)$, namely $C_0(V_{dc} = 0) \approx 3.35$ aF. However, a more powerful method is represented by multi-physics simulations performed with COMSOL®, as explained in the following.

B. Multi-Physics Simulations of a VACNT Matrix

Using the finite element method (FEM) in COMSOL Multiphysics®, the capacitance of a periodic structure of CNTs was calculated, namely deploying the Electro-Mechanical Module inside the tool. The periodicity of the structure allows working with a unit cell formed by 2×4 CNTs (Fig. 2). A 2×2 CNT matrix placed in the center of the unit cell is grounded, whereas the other 4 CNTs are connected to a variable dc bias voltage V_{dc}. The variation of the electric potential between two adjacent ground and signal electrodes produces a mechanical force that acts on the structure by deforming it, hence modifying the total capacitance.

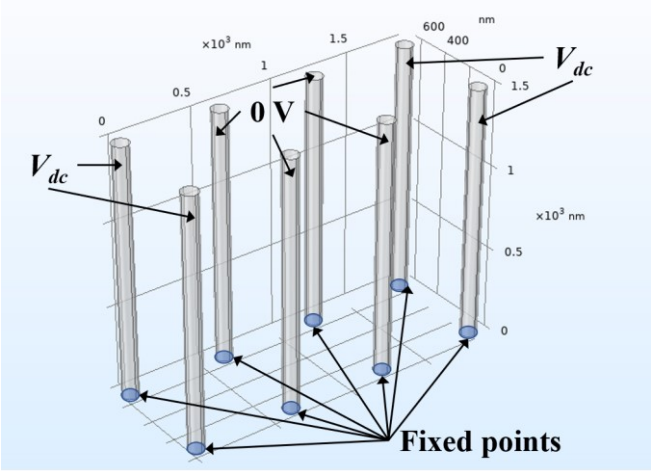

Fig. 2. 3D schematic of the unit cell simulated in COMSOL Multiphysics.

Three simulations were performed for three different CNT heights: 1 μm, 1.5 μm and 2 μm. The mechanical properties of the CNTs were chosen as follows: Young's modulus = 75 GPa, Poisson ratio = 0.28, and density = 1500 kg/m^3. The Young's modulus can be estimated by the Hall-Petch model, measuring the crystallinity of the CNTs by means of the Scherrer equation:

$$L_a = K\lambda/[\Delta(2\theta)cos\theta] \quad (4)$$

where L_a is the crystallite size, K is a dimensionless shape factor close to unity, λ is the wavelength of diffracted radiation, $\Delta(2\theta)$ is the line broadening, and θ is the angle of diffraction (or Bragg angle). The radius of each CNT is 50 nm and the gap between two adjacent CNTs is 500 nm. From preliminary measurements, L_a = 5.3 nm and, using the Hall-Petch model [32], we could estimate the value of Young's modulus to be 75 GPa. As regards the boundary conditions, the bottom section of each CNTs is fixed mechanically (thus allowing their bending with respect to the vertical axis) and the electric potential is varied in each simulation for V_{dc} = 0–100 V, with steps of 10 V. In Table I we show the pull-in voltage $V_{PULL\text{-}IN}$ (i.e., the threshold voltage beyond which the tips of two adjacent CNTs touch each other), the maximum displacement δ_{MAX}, and the minimum/maximum capacitance C_{MIN}/C_{MAX} for each value of the CNT height h; one can see that it was not possible to find the value of $V_{PULL\text{-}IN}$ in the first case (h = 1 μm), meaning that the mechanical stiffness of the CNTs prevents them from pulling in up to 100 V. As expected, the values of $V_{PULL\text{-}IN}$ decrease when increasing the h, whereas the values of δ_{MAX} and C_{MIN}/C_{MAX} increase, as it can be seen in Fig. 3, which represents the normalized capacitance as a function of V_{dc}. The most relevant outcome is that, increasing h of the CNTs, one can obtain steeper variations of the capacitance at lower dc bias voltage values.

TABLE I
MECHANICAL AND ELECTRICAL PERFORMANCE OF THE 2×4 CNT MATRIX SIMULATED IN COMSOL MULTIPHYSICS

h (μm)	$V_{PULL\text{-}IN}$ (V)	δ_{MAX} (nm)	C_{MIN} for V_{dc} = 0 V (10^{-2} fF)	C_{MAX} for $V_{dc} = V_{PULL\text{-}IN}$ (10^{-2} fF)
1	Over 100 V	20	4.024	4.101 (at 100 V)
1.5	47.37	24	5.742	5.873
2	31.58	30.5	7.453	7.695

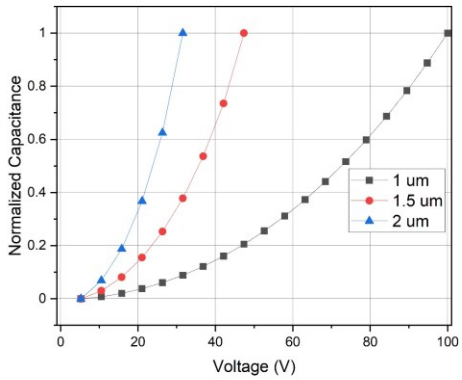

Fig. 3. Simulated normalized capacitance of the 2×4 CNT matrix, as a function of the applied dc bias voltage, for three values of the CNT height.

Finally, in Fig. 4 the mechanical displacement of the CNTs is shown in the case of CNTs with a height h = 2 μm. This figure gives the proof of the physical principle upon which the VACNT-based variable capacitor relies, i.e., the mechanical actuation of adjacent CNTs under an electrical excitation.

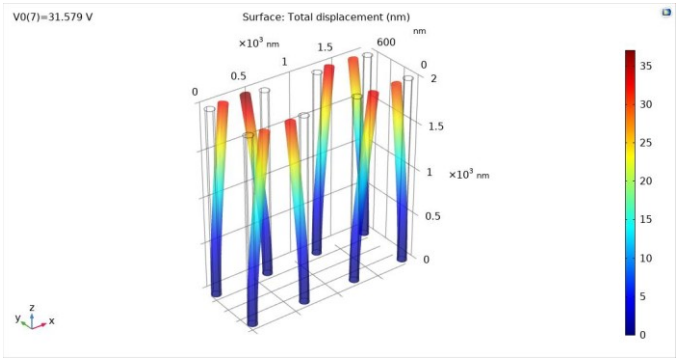

Fig. 4. Simulated mechanical displacement of the 2×4 CNT matrix under an electrical excitation, for the case of CNTs with a height h = 2 μm.

III. CIRCUIT AND 3D FULL-WAVE EM SIMULATIONS OF THE VACNT-BASED IDC AND FILTERS

A. Basic Requirements and Adopted Strategy for Design

Starting from the theoretical model and multi-physics simulations presented in Section II, the proposed CNT-based filter needs fulfill four requirements: (i) reconfigurability (i.e., the possibility of switching among a low-pass, a high-pass, or a band-pass topology); (ii) low dc bias voltage (V_{dc}) values to achieve the tunability of the filtering frequency; (iii) standard fabrication process (for CMOS compatibility); (iv) miniaturization for ease of integration. The solution adopted for the reconfigurability was the realization of a band-pass filter putting in cascade a low-pass filter and a high-pass filter. Between them, a Single Pole Double Throw (SPDT) switch selects the appropriate path between the input and output ports (to be implemented separately, e.g., of the type described in [33], [34]; nevertheless, this is out of the scope of the present work). As regards filters' tunability, from the theoretical model we estimated that a maximum V_{dc} of 8 V would be enough to maximize C_{tot} in (3). The most critical issues are (iii) and (iv). A standardization of the fabrication process is a crucial

prerequisite for large-scale production, which needs an extensive measurement campaign for high technology readiness level (TRL) validation. For this reason, the proposed filters were designed and fabricated using 300-µm-thick 4-inch wafers of high-resistivity silicon (HRSi); furthermore, exploiting CPW technology allows performing extensive on-wafer characterization using a standard probe station. Last, miniaturization represents a target in any more-than-Moore technological advancement, in which a high integration density is always a highly desirable achievement. Nevertheless, a filter with both high Q-factor and small size is very challenging, since the miniaturization (and successive integration) has a twofold effect: (i) degradation of unloaded Q-factors of microwave resonators; (ii) appearance of undesired parasitic effects. For all the latter reasons, higher values of IL than bulk components are expected, which often requires a post-amplification stage.

B. Circuit/EM Model and Simulations of the Low-Pass, High-Pass and Band-Pass Filters

The first step was the implementation of the circuit model (AWR Microwave Office®) for each of the two basic filters (i.e., low-pass and high-pass) based on lumped elements. The second step was the translation of the two circuits into their 3D full-wave EM versions (CST Microwave Studio®) using CPW lines to account for all the parasitic effects and EM couplings occurring at microwaves. The major constraint in designing such filters was the need of using IDCs with VACNTs as tuning elements, which entails a careful choice of the topology apt to guarantee the proper and easy polarization of the VACNTs themselves. Besides this aspect, another important and envisaged requirement was the possibility of biasing the VACNT-based IDCs independently, thus ensuring the maximum degree of freedom in tuning the filters. Hence, each basic filter was realized by means of a T-like topology, consisting of two series inductances and a shunt variable capacitor for the low-pass filter, and of two series variable capacitors and a shunt inductor for the high-pass filter. This is shown in Figs. 5a-c, in which we have also included the 3D EM layout for each filter in CPW technology; in this respect, the characteristic impedance was set to the standard 50 Ω value using gap-signal-gap dimensions of 60–100–60 µm, respectively. The reference substrate is 300-µm-thick HRSi/2-µm-thick silicon oxide (SiO_2), whereas the metallization is a 500-nm-thick gold (Au) layer. As regards the VACNT-based IDC, it is shown in Fig. 5a (3D design by CST Microwave Studio and, inset, cross-section with the different layers). Each of them is made of 250 digits, each digit having a width w_d of 250 nm and the gap g_d between two adjacent digits being 200 nm. The total length of each IDC is 100 µm; since each CNT has a diameter of 100 nm (with a height $h \approx 1.5$–2 µm) and the distance between two consecutive CNTs on the same digit is 500 nm, the total number of VACNTs for each IDC is about 37500. Therefore, from Fig. 1 one can deduce that $2d = 350$ nm. The dimensions w_d and g_d were constraint by technological issues, since the metallization used for the IDC is a 100-nm-thick molybdenum (Mo) layer. This thickness, together with the high melting temperature of molybdenum (2893.15 K), are essential prerequisites for proper CNT growth. However, molybdenum has a conductivity $\sigma_{Mo} = 1.82\times10^7$ S/m, hence 2.5×times less than gold conductivity. For these reasons, we can expect a degradation of filters' performance at microwaves due to thin metal losses (skin depth effect). The equivalent circuit of the IDC is presented in Fig. 5b: C_P is the capacitance between the IDC and the ground planes of the CPW, C_S is the equivalent series capacitance (which comprises the capacitance of the standalone IDC and the capacitance due to the VACNT matrix), L_S is the equivalent series inductance, and R_S is the equivalent series resistance. To have the desired band-pass filtering within the 4–16 GHz frequency range, the two meander-type series inductors of the low-pass filter have a theoretical inductance of 0.79 nH, whereas the meander-type shunt inductor of the high-pass filter has a theoretical inductance of 0.3 nH. In Fig. 5b, $C_P = 0.03$–0.15 pF, $R_S = 10$–50 Ω, $L_S = 0.01$–1 nH and $C_S = 0.01$–1 pF.

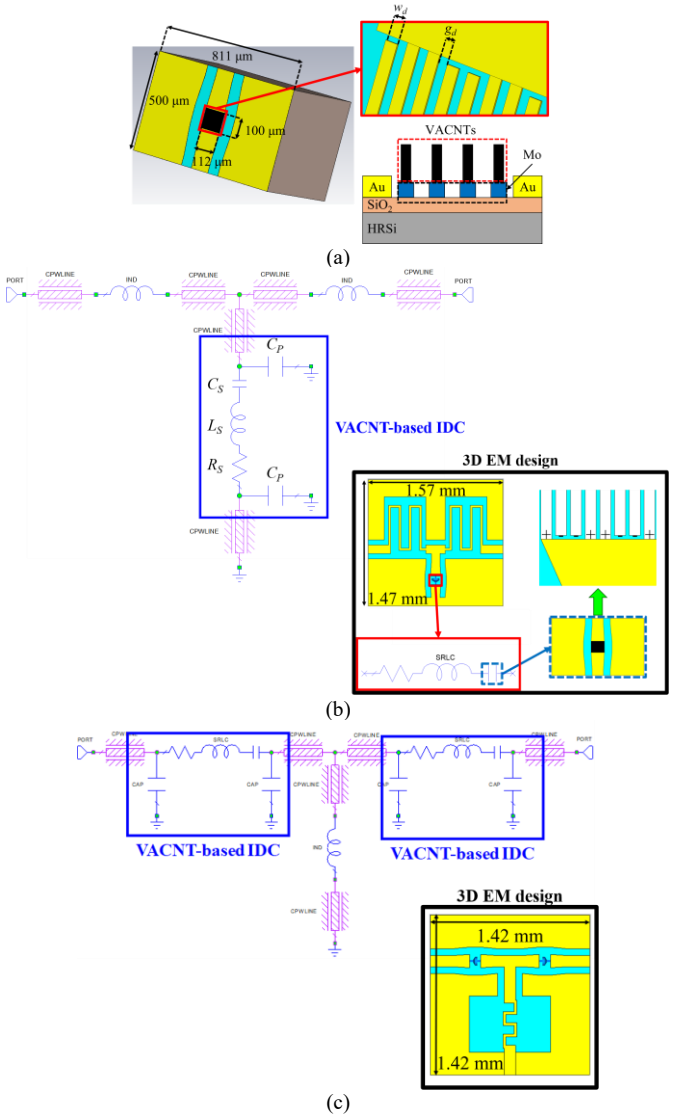

Fig. 5. (a) 3D design by CST Microwave Studio® of the VACNT-based IDC with main dimensions (insets: magnification of the digits' area, up, and cross-section with the different layers, down); circuit layout of (b) low-pass and (c) high-pass filter. In the black insets, the 3D EM layout is displayed for each filter.

The main key performance indicators (KPIs) of the two

filters are summarized in Table II (low-pass filter) and Table III (high-pass filter), respectively. For the low-pass filter, the selected KPIs are the 3-dB cut-off frequency f_C, the roll-off rate ζ_{-20dB} (referred to -20 dB), the relative stopband bandwidth *RSB*, the suppression factor *SF* (i.e., the rejection of the stopband), the normalized circuit size factor *NCS* represented by λ_g (the guided wavelength at f_C), and the architecture factor *AF*, which is equal to 1 for two-dimensional (2D) circuits, whereas it is equal to 2 for 3D circuits. The KPIs are defined as follows:

$$\zeta_{-20dB} = (\alpha_{-20dB} - \alpha_C)/(f_{-20dB} - f_C) \quad (5)$$

$$RSB = \frac{stopband\ bandwith}{stopband\ center\ frequency} \quad (6)$$

$$NCS = \frac{dimensions\ (widht \times length)}{\lambda_g^2} \quad (7)$$

where α_C and α_{-20dB} are the attenuation points (at the cut-off frequency and at -20 dB, respectively), and f_{-20dB} is the 20-dB stopband frequency. The total figure of merit *FOM* is:

$$FOM = (\zeta \times RSB \times SF)/(NCS \times AF). \quad (8)$$

Other KPIs of interest are the minimum in-band *IL* and the maximum in-band return loss. It is apparent from Table II that the *FOM* also changes when varying C_S, as expected. More in detail, the *FOM* increases for increasing values of C_S.

As regards the high-pass filter, we will consider the 3-dB cut-off frequency f_C, the 3-dB upper cut-off frequency f_{UP}, the roll-off rate ζ_{-40dB} (referred to -40 dB), the relative passband bandwidth *RPB* (which is defined in a way similar to *RSB*, but considering the passband instead of the stopband), the normalized circuit size factor *NCS*, the architecture factor *AF*, the minimum in-band *IL* and the maximum in-band return loss. In this case, ζ_{-40dB} is better than ζ_{-20dB} (for the low-pass filter), but the maximum in-band *IL* is higher, due to the series connection of the two VACNT-based IDCs. This aspect will reflect into the performance of the band-pass filter resulting from the cascade of the low-pass and high-pass filters.

We stress here that, for each type of filter, we chose selected values of C_S that provide the most significant performance, as one can see from Table II and Table III.

TABLE II
PERFORMANCE OF THE SIMULATED LOW-PASS FILTER AS A FUNCTION OF IDC'S CAPACITANCE

KPI	C_S = 0.05 pF	C_S = 0.1 pF	C_S = 0.15 pF
3-dB cut-off frequency f_C (GHz)	14.59	12.45	10.82
Roll-off rate ζ_{-20dB} (dB/GHz)	2.23	2.75	3.08
RSB	1.36	1.45	1.52
SF	1.5	1	1
NCS	0.04	0.03	0.02
AF	1	1	1
FOM	113.73	132.92	234.08
Minimum in-band *IL* (dB)	< 0.01	< 0.01	< 0.01
Maximum in-band return loss (dB)	35.48	29.87	27.91

TABLE III
PERFORMANCE OF THE SIMULATED HIGH-PASS FILTER AS A FUNCTION OF IDC'S CAPACITANCE

KPI	C_S = 0.15 pF	C_S = 0.25 pF	C_S = 0.35 pF
3-dB cut-off frequency f_C (GHz)	9.91	8.95	8.77
3-dB upper cut-off frequency f_{UP} (GHz)	40.06	37.67	36.69
Roll-off rate ζ_{-40dB} (dB/GHz)	5.54	5.6	5.38
RPB	1.21	1.23	1.23
NCS	0.02	0.01	0.01
AF	1	1	1
Minimum in-band *IL* (dB)	2.04	1.99	2.02
Maximum in-band return loss (dB)	39.19	42.23	26.13

The translation of the circuits shown in Fig. 5 into their 3D EM counterpart provides mostly the same results in terms of both reflection ($|S_{11}|$ or $|S_{22}|$) and transmission ($|S_{21}|$ or $|S_{12}|$) coefficients, thus giving the proof of the correct approach in designing the filters (as circuit and EM simulations should offer comparable outcomes). For this reason, in Fig. 6a-b we show the curves obtained for the low-pass and high-pass filters, respectively, as a function of the capacitance C_S. It is apparent how both $|S_{11}|$ and $|S_{21}|$ can be tuned by simply changing the values of C_S, namely the level of dc bias voltage applied to the VACNT matrix. When putting in cascade the low-pass and high-pass filters, we obtain the final 3rd-order band-pass filter, for which Fig. 6c shows $|S_{11}|$ and $|S_{21}|$ for some combinations of values of C_S (low-pass/high-pass, respectively). It is worth mentioning the importance of having VACNT matrixes that can be biased independently, as this confers a further degree of freedom in tuning the band-pass filter resonance. For example, it can be seen in Fig. 6c that the minimum of $|S_{11}|$ can be shifted of about 2 GHz (from 10.6 GHz down to 8.6 GHz), while keeping a large 3-dB fractional bandwidth (FBW_{-3dB}) in the range 52–62%. At the same time, the minimum in-band *IL* is in the range 2.2–3.7 dB, the maximum in-band return loss is between 18 dB and 37 dB, the maximum rejection in the band of interest (4–16 GHz) is in the range 15–30 dB, and the maximum roll-off rate ζ_{-20dB} is between 3.2 dB/GHz and 3.4 dB/GHz.

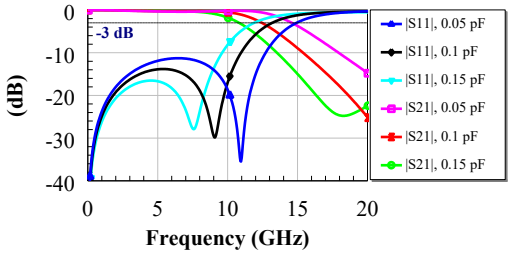

(a)

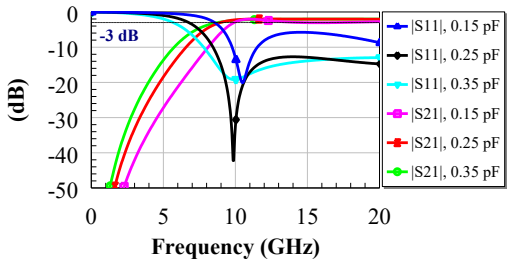

(b)

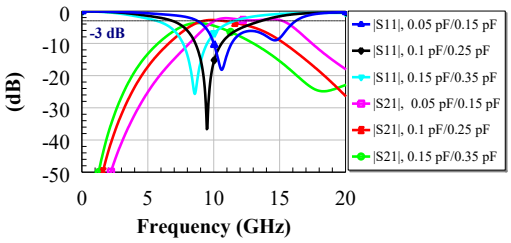

(c)

Fig. 6. Circuit/EM simulated reflection coefficient $|S_{11}|$ and transmission coefficient $|S_{21}|$ of the (a) low-pass filter, (b) high-pass filter, and (c) band-pass filter, as a function of different values of the VACNT-based IDCs.

We also performed an analysis of the influence of R_S and L_S (Fig. 5b) on the performance shown in Fig. 6 or, in other words, we studied the impact of the losses due to (also non-predictable) ohmic and inductive effects in the VACNT-based IDCs. In particular, we observed that: (i) for the low-pass filter, keeping L_S fixed, a change in R_S causes an increasing impedance mismatch to 50 Ω (i.e., the reflection coefficient worsens with more than 5 dB), whereas keeping R_S fixed, a change in L_S causes a down-shift of the minimum of $|S_{11}|$ with almost 700 MHz; (ii) for the high-pass filter, the most significant effect is due to R_S, because the two VACNT-based IDCs are put in series. For example, the *IL* at 10 GHz increases with more than 3 dB and the reflection coefficient is affected as well, with the minimum of $|S_{11}|$ shifting with more than 200 MHz. Consequently, when measuring the fabricated filters, we could expect significant differences with respect to the simulated performance, depending on the real values of R_S, L_S, and C_S.

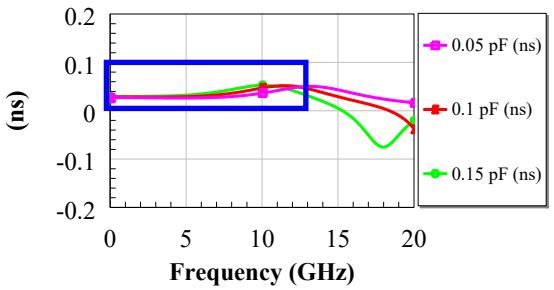

(a)

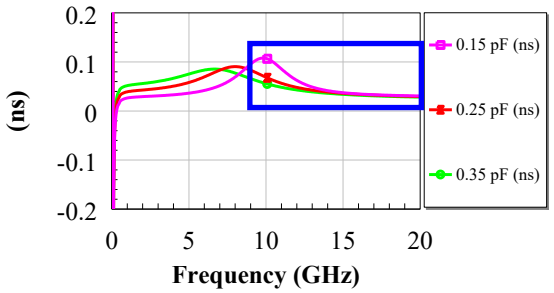

(b)

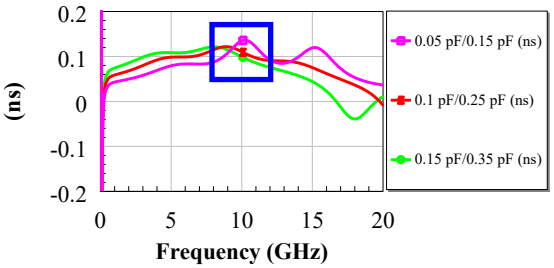

(c)

Fig. 7. Simulated group delay τ_g of the proposed VACNT-based (a) low-pass, (b) high-pass and (c) band-pass filters. The blue rectangles identify the passbands of interest.

Another KPI widely exploited to characterize the performance of a filter is the group delay τ_g (Fig. 7 for the three designed filters). As one can notice in Fig. 7, τ_g is small and quite flat in the passband of both the low-pass and high-pass filters (blue rectangles in Figs. 7a-b), as expected for a simple circuit; in the case of the high-pass filter (Fig. 7c), the frequency response of τ_g shows a variation of maximum 50% in the X band (blue rectangle). τ_g is negative (low-pass and band-pass filters) where the slope of the phase shift is positive, but this occurs out of the passbands, where the behavior of τ_g is of no interest.

The final EM design of the three filters is shown in Fig. 8, in which the main dimensions are W_{LPF} = 1.57 mm, H_{LPF} = 3.02 mm, W_{HPF} = 1.62 mm, H_{HPF} = 3.07 mm, W_{BPF} = 3.19 mm, and H_{BPF} = 3.47 mm. Referring to the free-space wavelength at 10 GHz (as the targeted frequency – included in all the passbands evidenced in Fig. 7 – for radar applications), it means that the three filters are strongly miniaturized, as they have overall dimensions (W × H) of just $\sim 0.05\lambda_0 \times 0.1\lambda_0$ (low-pass and high-pass filters) and $\sim 0.11\lambda_0 \times 0.12\lambda_0$ (band-pass filter). The red rectangles identify the (tunable) decoupling interdigitated capacitors $C_{DEC,1}$ and

$C_{DEC,2}$, to provide the dc bias voltage correctly. More in detail, $C_{DEC,1} \approx 1$ pF and $C_{DEC,2} \approx 0.3$ pF guarantee that the RF signal propagating inside the filters is decoupled from the dc bias voltage through the high-impedance $\lambda_g/4$-long lines (where λ_g is the guided wavelength at 10 GHz) connecting each VACNT-based IDC to the corresponding decoupling capacitor. This way, it is possible to bias independently the three VACNT matrixes, which ensures the full exploitation of filters' tunability properties. The two decoupling capacitors are adjustable (in the sense that their value can be increased by soldering – if needed – the lateral parts that are separated by thin channels from the main structures – blue rectangles in Fig. 8) and, despite their narrow-band behavior, they fit the requirements needed in the band of interest.

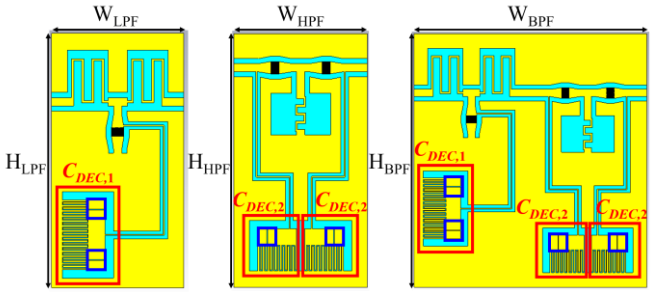

Fig. 8. EM layout of the (left) low-pass, (center) high-pass and (right) band-pass filters. Red rectangles: decoupling capacitors; blue rectangles: thin channels to adjust the capacitance of the decoupling capacitors.

IV. Fabrication of the VACNT-based IDCs and Filters

The VACNT-based filters were fabricated using classical micro- and nano-fabrication facilities. The fabrication process is described visually in Fig. 9.

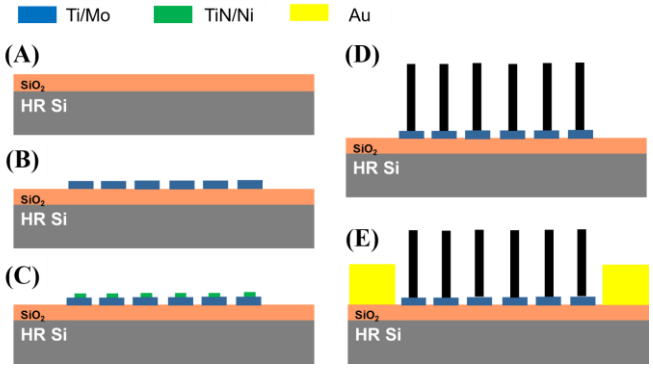

Fig. 9. Fabrication process flow of the VACNT-based filters.

First, a 2-µm-thick layer of SiO_2 obtained by thermal oxidation was deposited on a 300-µm-thick HRSi wafer, which is a standard passivation technique for CMOS processes to protect the silicon wafers from external contaminants (step A). The electrodes of each IDC were defined by e-beam lithography, then two thin layers of titanium (for adhesion) and molybdenum (10-nm-thick Ti/100-nm-thick Mo) were deposited successively by evaporation (step B). The metallization of electrodes was chosen to be molybdenum because it can withstand the high temperature necessary in the plasma process for the growth of the VACNTs. Then, the deposition of the catalyst dots, with a diameter of 200 nm and aligned along each IDC's electrode, was obtained by e-beam lithography, followed by the deposition of a thin layer of titanium nitride/nickel (15-nm-thick TiN/7-nm-thick Ni) by sputtering and evaporation, respectively (step C). Individual vertically aligned CNTs were grown by plasma enhanced chemical vapor deposition (PECVD) of acetylene and ammonia at 700°C (step D). The final step E concerned the deposition (by evaporation) of the gold metallization for the CPW-based structures and lines (in typical RF applications, a minimum thickness of 500 nm is needed). For this purpose, the CPW lines were defined by optical lithography. The challenge here is to make this step compatible with the presence of CNTs. All the experimental conditions were especially developed to avoid any damage of the nanotubes. In this case, the choice of the resist (thickness, viscosity, bake temperature), resist development after UV insolation, and lift-off process were carefully studied, which made it possible to obtain gold CPW lines with vertically aligned CNTs. The optical microscopy images of the fabricated low-pass, high-pass and band-pass filters are shown in Fig. 10, together with the basic components (meander inductors and VACNT-based IDC). Additional gold wires were soldered to connect electrically the floating ground plane to the major ground plane, as to avoid spurious wave propagation.

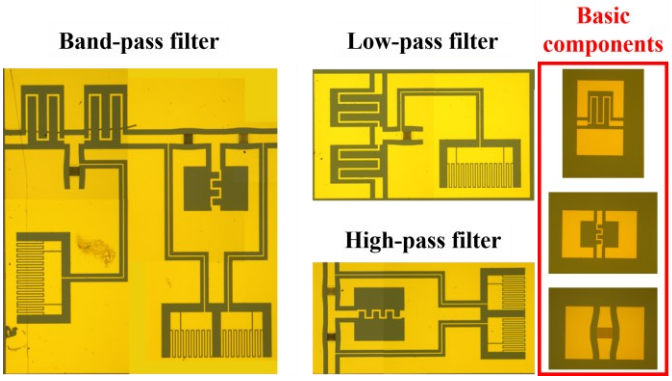

Fig. 10. Optical microscopy images of the different types of VACNT-based filters and (red inset) of the basic components (meander inductors and IDC).

The scanning electron microscopy (SEM) images of the VACNT matrix are shown in Fig. 11, from which one can see the uniformity of the CNT growth with a height h ~2 µm. The good alignment of the CNTs on the IDC is evident in the most-right picture. This condition is essential to guarantee the proper actuation of the VACNTs when applying a dc bias voltage.

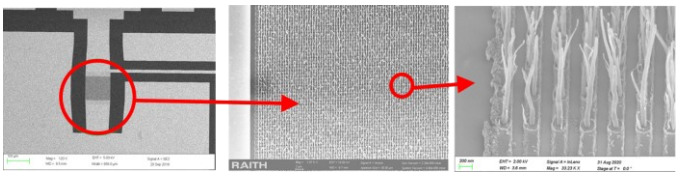

Fig. 11. SEM images of the VACNT matrix of an IDC.

V. Complete DC and RF Characterization of the VACNT-based Filters

The measurements of the VACNT-based filters were carried out using a vector network analyzer (VNA, Anritsu 37397D), together with a standard Short-Open-Load-Thru (SOLT)

calibration kit. A dc source (Agilent E3631A) was connected to the VNA to bias the three VACNT matrixes. First, we measured the basic components shown in Fig. 10, namely the series and shunt meander inductors (top and center structures in the red inset of Fig. 10), and the IDC (bottom structure in the red inset of Fig. 10). The extracted equivalent resistance and inductance of the two types of meander inductors are displayed in Fig. 12a, whereas Fig. 12b presents the comparison between the modelled and measured scattering (S) parameters of the single IDC without VACNTs.

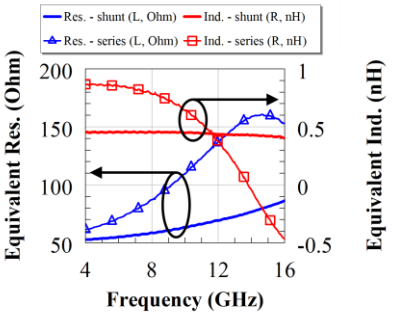

(a)

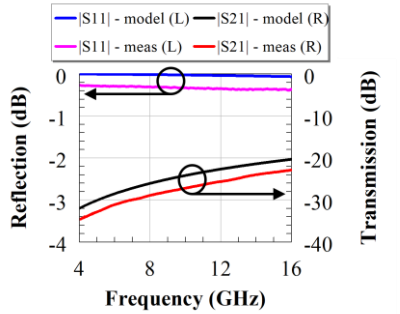

(b)

Fig. 12. (a) Extracted equivalent resistance (solid blue curves, left vertical axis) and equivalent inductance (solid red curves, right vertical axis) of the meander inductors; (b) comparison between modelled (solid blue and black curves) and measured (solid pink and red curves) of the reflection (left vertical axis) and transmission (right vertical axis) coefficients of the IDC without VACNTs.

From Fig. 12 we can deduce the following: (i) the series meander inductor (low-pass filter) exhibits an equivalent inductance between 0.37 nH and 0.87 nH in the frequency range 4–12 GHz, and it remains positive up to 13.79 GHz (i.e., the behavior of this component is inductive in the passband of interest, see Fig. 7a); (ii) as regards the shunt meander inductor (high-pass filter), the equivalent inductance is practically constant and equal to ~0.4 nH over the whole 4–12 GHz band, since the parasitic capacitances between the meander are very small; (iii) since a rigorous model of each meander inductor has to take also a resistive contribution into account, the equivalent resistance associated to the series inductor is between 60 Ω and 160 Ω, whereas the equivalent resistance associated to the shunt inductor spans the range 50–90 Ω. Hence, we can predict a degradation of the *IL*, especially in the case of the band-pass filter, due to an increased mismatch to the characteristic impedance of the CPW lines. Regarding Fig. 12b, it gives important information about the contribution of the sole IDC to the total capacitance C_S of the variable capacitors, since the capacitance of the VACNT matrix can be modelled as a tunable capacitance in parallel with the fixed capacitance of the standalone IDC, which is estimated to be about 0.01 pF by fitting the measurements with the equivalent circuit in Fig. 5b. Other parameters of interest resulting from the fitting are $C_P = 0.03$ pF, $R_S = 30$ Ω, and $L_S = 0.01$ nH; these values provide a good agreement with the measured S-parameters, as it can be seen from Fig. 12b. When extracting the equivalent circuit parameters of the IDC with the VACNT matrix as a function of the dc bias voltage, it is necessary to consider the intercorrelation among R_S, L_S, and C_S, due to the presence of parasitic effects generated by many factors, like CNT resistance and kinetic inductance [35], defects in CNT growth and alignment, potential short-circuits among adjacent electrodes and/or neighbor CNTs, unavoidable oxidation process of the thin Mo layer, etc. However, it is possible to provide a quite reliable range of values for R_S, L_S, and C_S when biasing the VACNT-based variable capacitor between 0 V and 8 V, as shown in Table IV (where the Q-factor is defined as $Q_f = (1/R_S)\sqrt{L_S/C_S}$). The expected degradation of Q_f must be considered as a potential cause for additional transmission losses. We stress here that the values presented in Table IV were extracted from the S-parameters of the single VACNT-based IDC, using the model shown in Fig. 5b and via a careful fitting process, by considering the same values extracted for the sole IDC without CNTs (see Fig. 12b)

TABLE IV
EXTRACTED PARAMETERS OF THE EQUIVALENT CIRCUIT OF THE VACNT-BASED IDC, AS A FUNCTION OF THE APPLIED DC BIAS VOLTAGE

dc voltage (V)	R_S (Ω)	L_S (nH)	C_S (pF)	*Q-factor*
0	36	0.1	0.5 (C_{min})	~0.4
8	48	0.1	0.65 (C_{max})	~0.26

From previous considerations, we can estimate the value of the variable capacitance provided by the sole VACNT matrix to be between 0.49 pF and 0.64 pF, hence an increase of about 77% when applying a dc bias voltage to the IDC or, in other words, $C_{max}/C_{min} \approx 1.3$. This result is remarkable, as it suggests the feasibility of tuning efficiently (and almost instantaneously, as the latency between the application of the biasing signal and the change in the capacitance is in the order of μs) each filter by applying a (relatively small) bias to the VACNT-based IDCs, and it represents the validation of the concepts stated in the Introduction and in Section II, namely the integration of CNT-based nanotechnology into CMOS-compatible passive microwave components with (relatively low-voltage) tunable characteristics. In the Appendix, we provide a more advanced method to model rigorously the VACNT-based IDC, as to take all the parasitic effects into account from a circuit point of view; this offers a practical and fast way to implement such a component in commercial software tools for RF design and project. Finally, the outcomes of the RF measurements performed on the three filters are shown in Fig. 13.

This article has been accepted for publication in IEEE Transactions on Nanotechnology. This is the author's version which has not been fully edited and content may change prior to final publication. Citation information: DOI 10.1109/TNANO.2022.3153561

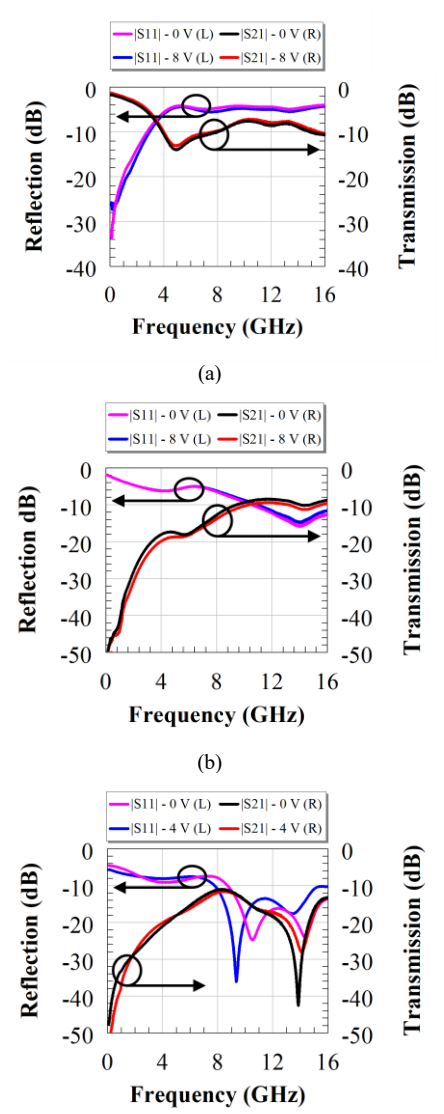

Fig. 13. Measured reflection (left vertical axis, solid pink and blue curves) and transmission (right vertical axis, solid black and red curves) coefficients, in the band 0–16 GHz, for the (a) low-pass filter, (b) high-pass filter and (c) band-pass filter, in the unbiased state (0 V) and for the maximum dc bias voltage applicable onto the VACNT-based IDCs.

For the sake of clarity, we present only the two main cases, i.e., unbiased filter (0 V) and filter biased with the maximum dc voltage apt to maximize the tunability effect. This dc bias voltage is equal to 8 V for the low-pass and high-pass filters, and to 4 V for the band-pass filter (because of the joint effects of the IDC-based resonators put in cascade). The working principle of the VACNT-based variable capacitor is validated, as it acts on both the reflection and transmission coefficients, with a very strong shift of the filtering frequency ($|S_{11}|$) in the case of the band-pass filter.

We stress here that, at dc bias voltage values higher than 8 V, a small current in the order of mA was detected to pass through the IDCs due to contacting of adjacent CNT tips inside the VACNT matrix. This phenomenon causes an undesired electrical charge of the touching CNTs; hence, a recovery time of some minutes was necessary to reset the electro-mechanical state of the CNTs. The combined effect of the actual values of R_S, L_S, and C_S gives rise to a different passband for the low-pass filter (Fig. 13a), which extends up to about 3 GHz. In the case of the high-pass filter (Fig. 13b), the passband covers the entire frequency range 8–16 GHz (as predicted by the simulations), but with an average value of the *IL* equal to 4 dB (a direct consequence of R_S and L_S). However, the most evident effect given by the tunable VACNT-based IDCs can be observed in Fig. 13c (band-pass filter): the maximum in-band return loss shifts of 1.16 GHz within the X band (from 10.51 GHz down to 9.35 GHz or, in other words, a tunability of 11.6% taking 10 GHz as reference frequency) and spans between 24.81 dB and 36.13 dB, whereas the maximum rejection is 31.65 dB; all the latter results are in good agreement with the performance predicted by the simulations. Nevertheless, the FBW_{-3dB} is 12.44%, the minimum in-band *IL* is between 11 dB and 12 dB (hence, the filter can be classified as a 'lossy' one [36]–[38]) with a maximum frequency shift of 220 MHz (tunability of 2.2%, likely due to undesired supplementary losses coming from the thin Mo layer and concealing the real transmission performance), and the maximum roll-off rate ζ_{-20dB} is within the range 1.7–2 dB/GHz. Finally, Fig. 14 shows the measured group delays τ_g for the three filters in the unbiased and biased states.

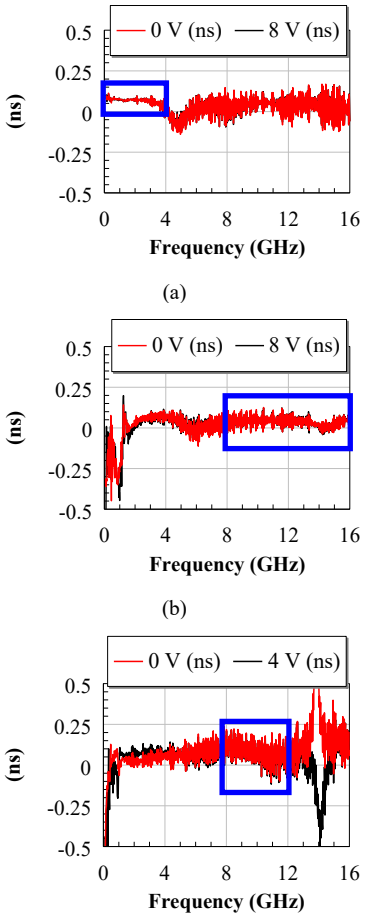

Fig. 14. Measured group delay τ_g of the proposed VACNT-based (a) low-pass, (b) high-pass and (c) band-pass filters. The blue rectangles identify the passbands of interest.

In agreement with the simulations presented in Fig. 7, the measured τ_g (which presents ripples coming from the frequency sampling of the RF measurements) is small and quite flat in the passband of both the low-pass and high-pass filters (blue rectangles in Figs. 14a-b); in the case of the high-pass filter (Fig. 14c), the frequency response of τ_g shows a small variation in the X band (blue rectangle). Again, τ_g is negative where the slope of the phase shift is positive, but this occurs out of the passbands in all the three cases, where the behavior of τ_g is of no interest.

We also investigated, by using SEM techniques (Fig. 15), the state of the VACNTs after the performed measurements to confirm the total recovery of the nanotubes after the electro-mechanical actuation. In this respect, the VACNTs do not show any evident structural modification or degradation due to the application of an external dc bias voltage. This ensures, in a first approximation, the reliability and endurance of the fabricated VACNT-based filters. Moreover, all measurements were performed at room temperature, and we expect that environmental conditions do not pose any problem; hence, no strict control of the temperature is required to preserve the achieved capacitance and losses.

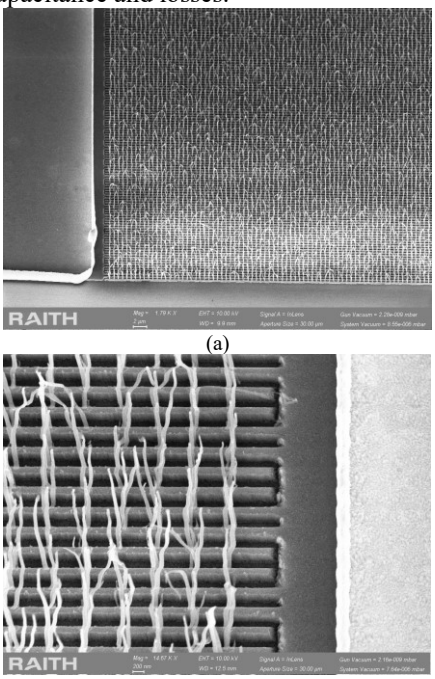

(a)

(b)

Fig. 15. SEM pictures of the generic VACNT-based IDC after measurements: (a) overview of the dense VACNT matrix; (b) detail with the digits of the IDC and the grown VACNTs.

Possible actions to counteract the effect of the losses could be the deposition of a thicker (i.e., up to 1 μm) layer of gold for the CPW lines, the optimization of the VACNT matrixes to further avoid growth defects and potential short-circuits, and the exploitation of state-of-the-art air bridges to connect the floating ground plane of the high-pass and band-pass filters (instead of using gold wires that introduce unpredictable parasitic inductances, due to the impossibility of control their length precisely). Also, the oxidation of the thin Mo layer has to be counteracted and, in this sense, new research is in progress (but at its very beginning) to find a feasible solution, together with the possibility of increasing the reproducibility of the fabrication yield by a state-of-the-art optimization of the CNT growth process. Despite the aforementioned limitations, the outcomes of the RF measurements represent, to the authors' knowledge, an unprecedented application of CNTs to create tuning components for microwave applications.

VI. Conclusion

In this manuscript we have presented the very first prototypes of tunable and miniaturized filters, whose voltage-controllable components consist of variable capacitors based on vertically aligned carbon nanotubes, for wireless applications targeting the C, X, and K_u bands (4–16 GHz). The electro-mechanical actuation of the carbon nanotubes has been investigated using theoretical principles and multi-physics simulations. Then, a set of circuit and electromagnetic simulations has been performed to design the three filters (low-pass, high-pass, and band-pass) and to predict their performance according to the envisaged behavior of the variable capacitors. Finally, a complete dc and RF characterization of the three filters has been discussed in detail, with a particular attention to advantages and disadvantages of the proposed solution, and to possible countermeasures apt to balance the drawbacks. To the authors' knowledge, this concept represents an unprecedented application of carbon nanotubes, that could pave the way for a novel class of tuning components in microwave engineering.

Appendix

The extraction of a rigorous equivalent circuit model for the VACNT-based IDC was done starting from the measured scattering matrix $\boldsymbol{S}$ of the component. A π network was designed, so, for simplicity, the scattering matrix was first converted into an admittance matrix $\boldsymbol{Y}$, as follows:

$$\boldsymbol{Y} = (\boldsymbol{I} - \boldsymbol{S})(\boldsymbol{I} + \boldsymbol{S})^{-1}/Z_0 = \frac{1}{Z_0}\begin{bmatrix} Y_{11} & Y_{12} \\ Y_{21} & Y_{22} \end{bmatrix} \tag{9}$$

where Z_0 is the normalization impedance used to compute the S-parameters, and, for symmetry, it must be $Y_{11} = Y_{22}$ and $Y_{12} = Y_{21}$. Only two different impedances in the π network must thus be designed, Z_π and Z_μ. They shall approximate the admittances Y_{ij} obtained from the measured data, in particular $Z_\pi \approx 1/(Y_{11}+Y_{21})$ and $Z_\mu \approx 1/Y_{21}$ at the frequencies of interest and be physically realizable.

A reasonable choice for the form of the Z_π and Z_μ impedances is a rational function, so that they can then be mapped to circuit components by the well-known partial fraction expansion technique:

$$\boldsymbol{Y}(s) = \frac{\sum_{i=0}^{N_b} b_i s^i}{\sum_{i=0}^{Na} a_i s^i} = k_1 s + k_0 + \sum_{i=1}^{N_a} \frac{r_i}{s - p_i} \tag{10}$$

where, to ensure physical realizability, it must be $|N_a – N_b| \leq 1$. r_i and p_i are the residues and poles, respectively, that in general can be either real or come in complex conjugate pairs. Each fraction corresponding to a real residue can be mapped immediately to a simple parallel RC branch, with all the fractions corresponding to a series of branches. Complex

conjugate pairs lead to resonant RLGC branches, but they were not needed in this specific case. k_1 and k_0 (an inductor and a resistor) can arise if $N_b \geq N_a$, but again, that was not the case for this system. Indeed, good results were achieved by using $N_a = 3$, $N_b = 2$ for the representation of Z_π and $N_a = 2$, $N_b = 1$ for the representation of Z_μ. The approximation was obtained using MATLAB's invfreqs function, which also guarantees stability of the fitted rational fraction by ensuring all poles have a negative real part, and then decomposed using the residue function, yielding the circuit shown in Fig. 16. The outcomes of the fitting procedure are displayed in Fig. 17 for both the amplitude and phase of Y_{11} and Y_{21}: the matching with the measured admittance parameters is excellent.

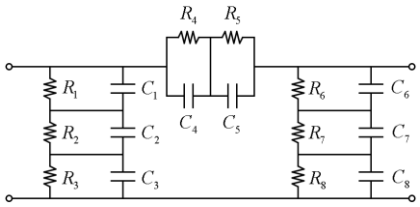

Fig. 16. Synthesized equivalent circuit of the VACNT-based IDC. $R_1 = 876.5\ \Omega$, $R_2 = 2.989\ k\Omega$, $R_3 = 26.97\ k\Omega$, $R_4 = 14.2\ k\Omega$, $R_5 = 1.581\ M\Omega$, $R_6 = 876.5\ \Omega$, $R_7 = 2.989\ k\Omega$, $R_8 = 26.97\ k\Omega$, $C_1 = 77.95$ fF, $C_2 = 77.14$ fF, $C_3 = 257$ fF, $C_4 = 8.946$ fF, $C_5 = 36.23$ fF, $C_6 = 77.95$ fF, $C_7 = 77.14$ fF, $C_8 = 257$ fF.

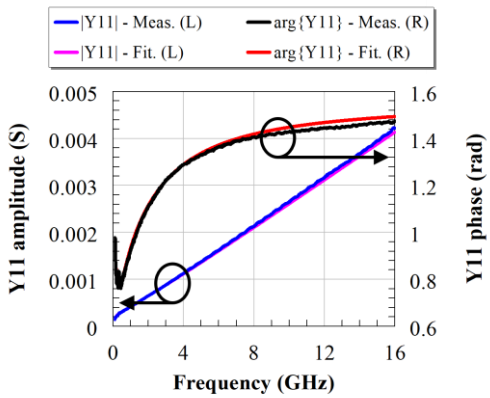

(a)

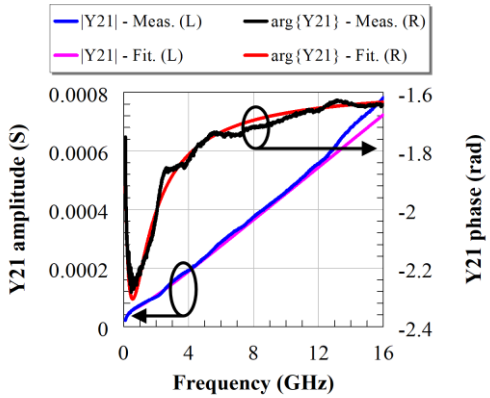

(b)

Fig. 17. Comparison between measured and modelled admittance parameters, in terms of amplitude (in Siemens, left vertical axis, solid blue and pink curves) and phase (in radians, right vertical axis, solid black and red curves) of the VACNT-based IDC at 0 V: (a) Y_{11}; (b) Y_{21}.

REFERENCES

[1] L. Zhu, S. Sun, and R. Li, "Microwave Bandpass Filters for Wideband Communications," in *Wiley Series in Microwave and Optical Engineering*, 1st ed., Hoboken, New Jersey, USA: John Wiley & Sons Inc., 2012.

[2] D.-S. Kim, D.-H. Kim, and S.-W. Yun, "Design of an active tunable bandpass filter for spectrum sensing application in the TVWS band," *J. Electromagn. Eng. Sci.*, vol. 17, no. 1, pp. 34–38, Jan. 2017.

[3] M. Yuceer, "A reconfigurable microwave combline filter," *IEEE Trans. Circuits Syst. II: Exp. Briefs*, vol. 63, no. 1, pp. 84–88, Jan. 2016.

[4] J. Bland-Hawthorn and G. Cecil, "Classical Spectroscopy," in *Experimental Methods in the Physical Sciences*, vol. 29, Part B, pp. 363–391, 1996.

[5] C. Kerbage, R. S. Windeler, B. J. Eggleton, M. Dolinskoi, P. Mach, and J. A. Rogers, "Tunable devices based on dynamic positioning of micro-fluids in microstructure optical fiber," *Opt. Commun.*, vol. 204, pp. 179–184, 2002.

[6] S. Dey and S. K. Kou, "Reliable, Compact, and Tunable MEMS Bandpass Filter Using Arrays of Series and Shunt Bridges for 28-GHz 5G Applications," *IEEE Trans. Microw. Theory Tech.*, vol. 69, no. 1, pp. 75–88, Jan. 2021.

[7] M. Bakri-Kassem, S, Fouladi, and R. R. Mansour, "Novel High-*Q* MEMS Curled-Plate Variable Capacitors Fabricated in 0.35-μm CMOS Technology," *IEEE Trans. Microw. Theory Tech.*, vol. 56, no. 2, pp. 530–541, Feb. 2008.

[8] A. C. Sanabria-Borbón and E. Sánchez-Sinencio, "Synthesis of High-Order Continuously Tunable Low-Pass Active-R Filters," *IEEE Trans. Circuits Syst. I Regul. Pap.*, Early Access. DOI: 10.1109/TCSI.2021.3055239.

[9] T. Lim, A. Anand, J. Chen, X. Liu, and Y. Lee, "Design Method for Tunable Planar Bandpass Filters With Single-Bias Control and Wide Tunable Frequency Range," *IEEE Trans. Circuits Syst. II: Exp. Briefs*, vol. 68, no. 1, pp. 221–225, Jan. 2021.

[10] X. Chen, T. Yang, and P.-L. Chi, "Novel Single-Ended-to-Balanced Filter With Reconfigurable Working Modes, Frequency, Bandwidth, and Single/Dual-Band Operations," *IEEE Access*, vol. 9, pp. 14216–14227, Jan. 2021.

[11] M. Fan, K, Song, L, Yang, R, and Gómez-García, "Frequency-Reconfigurable Input-Reflectionless Bandpass Filter and Filtering Power Divider With Constant Absolute Bandwidth," *IEEE Trans. Circuits Syst. II: Exp. Briefs*, Early Access, Jan. 2021, DOI: 10.1109/TCSII.2021.3049417.

[12] A. Zakharov, S. Rozenko, and M. Ilchenko, "Varactor-tuned microstrip bandpass filter with loop hairpin and combline resonators," *IEEE Trans. Circuits Syst. II: Exp. Briefs*, vol. 66, no. 6, pp. 953–957, Jun. 2019.

[13] W. Qin, J. Cai, Y.-L. Li, and J.-X. Chen, "Wideband tunable bandpass filter using optimized varactor-loaded SIRs," *IEEE Microw. Wirel. Compon. Lett.*, vol. 27, no. 9, pp. 812–814, Sep. 2017.

[14] H.-Y. Tsai, T.-Y. Huang, and R.-B. Wu, "Varactor-tuned compact dual-mode tunable filter with constant passband characteristics," *IEEE Trans. Components, Packag. Manuf. Technol.*, vol. 6, no. 9, pp. 1399–1407, Sep. 2016.

[15] G. Suo *et al.*, "Low loss tunable superconducting dual-mode filter at L-band using semiconductor varactors," *IEEE Microw. Wirel. Compon. Lett.*, vol. 24, no. 3, pp. 170–172, Mar. 2014.

[16] C. Li *et al.*, "A tunable high temperature superconducting bandpass filter realized using semiconductor varactors," *IEEE Trans. Appl. Supercond.*, vol. 24, no. 5, pp. 1–5, Oct. 2014.

[17] P. Bouça, R, Figueiredo, J. N. Matos, P, M. Vilarinho, and N. Borges Carvalho, "Intermodulation Distortion Analysis of Microwave Tunable Filters Using Barium Strontium Titanate Capacitor and Varactor Diode," in *Proc. 15th European Microwave Integrated Circuits Conference (EuMIC)*, Utrecht, Netherlands, 2021, DOI: 10.1109/EuMIC48047.2021.00063.

[18] M. Aldrigo, M. Dragoman, S. Iordanescu, F. Nastase, and S. Vulpe, "Tunable Microwave Filters Using HfO_2-Based Ferroelectrics," *Nanomaterials*, vol. 10, 2020, Art. no. 2057.
[19] T. B. Herbert, J. S. Hyland, S. Abdullah, J. Wight, and R. E. Amaya, "An Active Bandpass Filter for LTE/WLAN Applications Using Robust Active Inductors in Gallium Nitride," *IEEE Trans. Circuits Syst. II: Exp. Briefs*, Early Access, Feb. 2021, DOI: 10.1109/TCSII.2021.3054739.
[20] X. Wu, M. Nafe, A. Álvarez Melcón, J. S. Gómez-Díaz, and X. Liu, "Frequency Tunable Non-Reciprocal Bandpass Filter Using Time-Modulated Microstrip $\lambda_g/2$ Resonators," *IEEE Trans. Circuits Syst. II: Exp. Briefs*, vol. 68, no. 2, pp. 667–671, Feb. 2021.
[21] H. Xu, Y, Wang, F. A. Ghaffar, and L. Roy, "Reconfigurable Microwave Filters Implemented Using Field Programmable Microwave Substrate," *IEEE Trans. Microw. Theory Tech.*, vol. 69, no. 2, pp. 1344–1354, Feb. 2021.
[22] Y.-H. Cho, C. Park, and S.-W. Yun, "0.7-1.0-GHz Switchable Dual-/Single-Band Tunable Bandpass Filter Using a Switchable J-Inverter," *IEEE Access*, vol. 9, pp. 16967–16974, Jan. 2021.
[23] L. Gao and G. M. Rebeiz, "A 0.97-1.53-GHz tunable four-pole bandpass filter with four transmission zeroes," *IEEE Microw. Wireless Compon. Lett.*, vol. 29, no. 3, pp. 195–197, Mar. 2019.
[24] L. Szydlowski, A, Lamecki, and M. Mrozowskitic, "Design of Microwave Lossy Filter Based on Substrate Integrated Waveguide (SIW)," *IEEE Microw. Wirel. Compon. Lett.*, vol. 21, no. 5, pp. 249–251, May 2011.
[25] L. Pierantoni, F. Coccetti, and P. Russer, "Nano-electronics: The paradigmshift," *IEEE Microw. Mag.*, vol. 11, no. 17, pp. 8–10, Dec. 2010.
[26] M. J. Biercuk, S. Ilani, C. M. Marcus, and P. L. McEuen, "Electrical transport in single-wall nanotubes," in *Carbon Nanotubes, Topics in Applied Physics*, vol. 111, A. Jorio, G. Dresselhaus, and M. S. Dresselhaus (Eds.), Berlin Heidelberg, Germany: Springer-Verlag, 2008, pp. 455–493.
[27] D. Dragoman and M. Dragoman, "Variable capacitance mechanisms in carbon nanotubes," *J. Appl. Phys.*, vol. 101, 2007, Art. no. 036111.
[28] T. Ricart, S. Pacchini, D. Dubuc, and K. Grenier, "Multiphysic modeling and design of carbon nanotubes based variable capacitors for microwave applications," in *Proc. 38th European Microwave Conference (EuMC)*, Amsterdam, Netherlands, 2008, DOI: 10.1109/EUMC.2008.4751672.
[29] D. V. Lioubtchenko, I. V. Anoshkin, I, I. Nefedova, J. Oberhammer, and A. V. Räisänen, "W-band phase shifter based on optimized optically controlled carbon nanotube layer," in *Proc. IEEE MTT-S International Microwave Symposium (IMS)*, Honololu, HI, USA, 2017, DOI: 10.1109/MWSYM.2017.8058815.
[30] A. A. Generalov, D. V. Lioubtchenko, and A. V. Räisänen, "Reconfigurable mm-wave phase shifter based on high impedance surface with carbon nanotube membrane MEMS," in *Proc. Global Symposium on Millimeter-Waves (GSMM)*, Montreal, QC, Canada, 2015, DOI: 10.1109/GSMM.2015.7175112.
[31] M. Aldrigo, M. Dragoman, S. Xavier, and A. Ziaei, "A novel tunable microwave filter based on carbon nanotubes varactors," in *Proc. International Semiconductor Conference (CAS)*, Sinaia, Romania, 2016, DOI: 10.1109/SMICND.2016.7783040.
[32] M. Kato, "Hall-Petch Relationship and Dislocation Model for Deformation of Ultrafine-Grained and Nanocrystalline Metals," *Mater. Trans.*, vol. 55, no. 1, pp. 19–24, 2014.
[33] M. Pustan, R. Chiorean, C. Birleanu, C. Dudescu, R. Muller, A. Baracu, and R. Voicu, "Reliability design of thermally actuated MEMS switches based on V-shape beams," *Microsyst. Technol.*, vol. 23, no. 9, pp. 3863–3871, Sep. 2017.
[34] C. Birleanu, M. Pustan, R. Müller, C. Dudescu, V. Merie, R. Voicu, and A. Baracu, "Experimental investigation by atomic force microscopy on mechanical and tribological properties of thin films," *Int. J. Mater. Res.*, vol. 107, no. 5, pp. 429–438, Apr. 2016.
[35] H. Li and K. Banerjee, "High-Frequency Analysis of Carbon Nanotube Interconnects and Implications for On-Chip Inductor," *IEEE Trans. Electron Devices*, vol. 56, no. 10, pp. 2202–2214, Oct. 2009.
[36] L. Szydlowski, A, Lamecki, and M. Mrozowskitic, "Synthesis of Coupled-Lossy Resonator Filters," *IEEE Microw. Wirel. Compon. Lett.*, vol. 20, no. 7, pp. 366–368, Jul. 2010.
[37] T. Yang and G. M. Rebeiz, "Tunable 1.25–2.1-GHz 4-Pole Bandpass Filter With Intrinsic Transmission Zero Tuning," *IEEE Trans. Microw. Theory Tech.*, vol. 63, no. 5, pp. 1569–1578, May 2015.
[38] L. Zappelli, "Equivalent Circuits of Lossy Two-Port Waveguide Devices" *IEEE Trans. Microw. Theory Tech.*, vol. 67, no. 10, pp. 4095–4106, Oct. 2019.

M. Aldrigo (M'12) received the Ph.D. in Electronic Engineering, Telecommunications, and Information Technology from the Faculty of Engineering, University of Bologna, Italy, in 2014. Since 2014, he is Principal Researcher III with IMT-Bucharest, Romania.

His main expertise comprises the electromagnetic simulation and experimental characterization of RF/microwave/millimeter-wave/THz systems for wireless/energy-harvesting applications embedding carbon-based, 2D, and nanoscale ferroelectric materials. He has co-authored more than 70 papers in ISI ranked journals and conferences. He is an IEEE member. He serves or has served as reviewer for many journals and as (co-)chair in international conferences.

M. Dragoman received the Ph.D. in electronics at the University "Politehnica" Bucharest, Romania, in 1991. In the period 1992-1994 he was the recipient of the Humboldt Fellowship award and followed postdoctoral studies at Duisburg University, Germany.

He is Senior Researcher I with IMT-Bucharest, Romania. He has co-authored more than 250 scientific papers in ISI ranked journals and conferences, and 6 monographies.

Prof. Dragoman was awarded the "Gheorghe Cartianu" prize of the Romanian Academy in 1999.

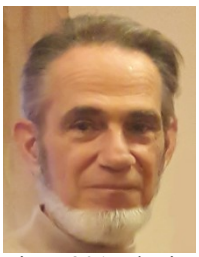

S. Iordanescu (M'91) graduated the Faculty of Electronics and Telecommunications at the Polytechnic Institute of Bucharest, Romania, in 1972, and received the Ph.D. degree in Electronic Engineering from the University "Politehnica" Bucharest, Romania, in 2000.

Since 2015, he is Senior Researcher with IMT-Bucharest.

He is the author of more than 100 scientific papers in peer-reviewed journals and conferences. His research interests include microwave SAW filter and sensor design, the

characterisation of dielectric and ferroelectric materials, and the design of various microwave and millimetre wave circuits. He received the "Tudor Tanasescu" Romanian Academy award (with team) in 2003.

G. Boldeiu graduated the Faculty of Electrical Engineering, Bucharest, Romania, in 2001, and Faculty of Physics. Bucharest, Romania, in 2014. In 2001 he was hired at IMT-Bucharest and between 2007 and 2017 he worked in the Simulation Laboratory as simulation engineer, being involved in the simulation of the electrical, mechanical, and thermal phenomena of MEMS devices. For a short period, 2017-2019, he worked as thermal simulation engineer at Continental, Timisoara, Romania. Here he developed and ensured thermal management for High Flash Lidar. In 2019 he returned to IMT and currently he activates in the L4 Laboratory.
Starting from 2020, he is Ph.D. student in the frame of the Faculty of Electronics, Telecommunications and Information Technology from University "Politehnica" Bucharest.

P. Crippa (M'02–SM'16) received the Laurea degree (summa cum laude) in Electronic Engineering from the Università degli Studi di Ancona, Ancona, Italy, in 1994, and the Ph.D. degree in Electronic Engineering from the Polytechnic of Bari, Bari, Italy, in 1999.
From 1999, he was a Research Assistant with the Polytechnic University of Marche (UnivPM), Ancona, Italy, where he has been an Assistant Professor with the Department of Information Engineering, since 2006, teaching courses in basic, analog, industrial, and power electronics. His current research interests include micro and nanoelectronics, statistical integrated circuit design and device modeling, mixed-signal and RF circuit design, signal processing, and neural networks. He has authored or co-authored over 110 papers in international journals, edited books, and conference proceedings.
He is currently an Associate Editor of the IEEE ACCESS and serves on the Editorial Boards/as reviewer of several scientific journals and conferences in the field of electronics, signal processing, and computational intelligence.
He is a member of the Associazione Italiana di Elettrotecnica, Elettronica, Automazione, Informatica e Telecomunicazioni (AEIT).

G. Biagetti (S'03–M'05) received the Laurea degree (summa cum laude) in Electronic Engineering in 2000, and the Ph.D. degree in electronics and telecommunications engineering in 2004, both of them from the Polytechnic University of Marche (UnivPM), Ancona, Italy, where he is currently an Assistant Professor, teaching digital electronics.
He has authored more than 80 scientific papers in peer-reviewed journals and conferences.
His current research interests include analog, digital, and mixed signal circuit design and simulation, embedded systems design, wireless systems and networks, and signal processing.

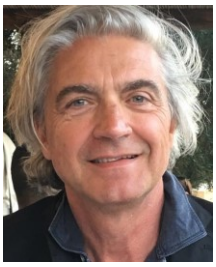

C. Turchetti received the Laurea degree in Electronic Engineering from the University of Ancona, Ancona, Italy, in 1979. He joined the Polytechnic University of Marche (UnivPM), Ancona, Italy, in 1980, where was the Head of the Department of Electronics, Artificial Intelligence and Telecommunications for five years and is currently a Full Professor of micro-nanoelectronics and design of embedded systems.
His current research interests include statistical device modeling, RF integrated circuits, device modeling at nanoscale, computational intelligence, signal processing, pattern recognition, system identification, machine learning and neural networks for embedded systems.
He has published more than 160 journal and conference papers, and two books. The most relevant papers were published in IEEE J. of Solid-State Circuits, IEEE Trans. on Electron Devices, IEEE Trans. on CAD of IC's and Systems, IEEE Trans. on Neural Networks and Learning Systems, IEEE Trans. on Signal Processing, IEEE Trans. on Cybernetics, IEEE J. of Biomedical and Health Informatics, IEEE Trans. on Consumer Electronics, Information Sciences.
He has held a variety of positions as Project Leader in several applied research programs developed in cooperation with small, large, and multinational companies in the field of microelectronics.
Prof. Turchetti has served as a Program Committee Member for several conferences and as a reviewer of several scientific journals. He is a Life Member of the IEEE, Computational Intelligence and Signal processing Society. He has been an Expert Consultant of the Ministero dell'Università e Ricerca.

L. Pierantoni is Full Professor of Electromagnetic Fields at the Polytechnic University of Marche (UnivPM), Ancona, Italy. He received (1988) the Laurea Degree (summa cum laude) in Electronic Engineering and the Ph.D. Degree (1993) in Electromagnetics from the University of Ancona, Italy. From 1996 to 1999, he worked at the Technical University of Munich, Germany, as Senior Research Scientist.
His research interests are in the development of computational techniques for the multi-physics modeling of nano-to-meso-scale devices/systems, including electrodynamics, quantum mechanics, thermal effects, and spintronics. Co-founder and first chair of the MTT-S "RF Nanotechnology" technical committee. IEEE MTT-S Distinguished Microwave Lecturer (DML, 2012-2014) and IEEE MTT-S DML Emeritus (DML-E, 2015-2016). IEEE Nanotechnology Council (NTC) Distinguished Lecturer (2015-2016). Member of the Nanotechnology Council (NTC) AdCom (since 2012). Member of the International Microwave Symposium Technical Program Committee. Senior Editor of the IEEE Trans. on

Nanotechnology (TNANO). Associate Editor of the Journal of Comp. Electronics (JCE, Springer), Nanomaterials and Nanotechnology (NMNT, InTech). EuMA Member. Member of the Italian Institute of Nuclear Physics (INFN). IEEE Senior Member. He is principal investigator in several European projects. He has (co-)authored about 300 papers in peer-reviewed journals and conferences.

D. Mencarelli received (2002) the Laurea in Electronic and Telecommunication Engineering from Polytechnic University of Marche (UnivPM), Ancona, Italy. He obtained the Ph.D. degree in Electronic and Telecommunication Engineering from the same university, in 2005. Since 2014, he is Assistant Professor at the Department of Information Engineering of UnivPM. His research activity spans over a wide area, including coherent charge transport in low dimensional systems, photonic crystals, nano-field effect transistors, planar slot array antennas and microwave components, Scanning Probe Microscopy, opto-mechanics and phononic devices. He is an IEEE MTT-S Speaker Bureau, a voting member of the Nanotechnology Council (NTC) AdCom, a member of the Italian Institute of Nuclear Physics (INFN), a member of the MTT TC 25 Technical Committee, an Associate Editor of Nanomaterials and Nanotechnology (NMNT, InTech), and of Journal of Comp. Electronics (JCE, Springer).

S. Xavier received the M.S. degree in Thin Layer and Surface Engineering from the University Louis Pasteur de Strasbourg (France) in 2005. He then pursued his scientific career with a Research and Technological Diploma from the University d'Evry-Val-d'Essonne (France) in 2007. He joined Thales Research & Technology in 2007 and his specialist field is the development of devices based on carbon nanotubes/2D materials for RF applications (antennas, filters, switches, etc.). Currently in the Technological and Advanced Characterization Lab, he is responsible of the Nanoelectronics topics and the associated research development. Over the past 14 years, he has been heavily involved in several European and national projects (NANORF, NANOSMART, Mercure, NANOCOM, Sims, Gospel, Opther, etc.).

L. Gangloff has been a research engineer at Thales Research and Technology in Palaiseau for over 10 years. After several years spent in charge of aspects related to the growth and integration of carbon nanotubes in devices, he is currently responsible for the field emission theme. He is author and co-author of more than 20 publications, and inventor or co-inventor of 6 patents in this field.

A. Ziaei received the B.S. degree in Electronic Engineering from the University of Paris XI (Orsay) in 1997, the M.S. degree in Electronic and Microwave Engineering from the University of Paris VI (Jussieu) in 1998, and he received the Ph.D. degree in microwaves from the Department of Electronic Engineering at CNRS-IEMN (Institut d'Electronique et de Microélectronique et de Nanotechnologie) in 2005. He joined Thales Research & Technology, France, in 2000 as research engineer. His research interests include the development, design, fabrication, and characterization of RF MEMS components, such as mechanical switches, transmission lines, etc. He was involved or in charge of many French or European projects: ARHMS, SATURNE, NANOPACK, NANOTEG, NANOTHERM, NANOCOM, NANOTEC, SMARTPOWER, SMARTEC, SMARTHERM, NANOSMART (project coordinator), NANOPOLY (project coordinator), etc. He is a member of IEEE.